Hybrid-PIC Simulation of Backsputtered Carbon Transport in the Near-Field Plume of a Hall Thruster

IEPC-2017-537

Presented at the 35th International Electric Propulsion Conference
Georgia Institute of Technology • Atlanta, Georgia • USA
October 8 – 12, 2017

Maria Choi,[1] John T. Yim,[2] George J. Williams,[3] and Daniel A. Herman[4]
NASA Glenn Research Center, Cleveland, OH, 44135, USA

James H. Gilland[5]
Ohio Aerospace Institute, NASA GRC, Cleveland, OH, 44135, USA

Magnetic shielding has eliminated boron nitride erosion as the life limiting mechanism in a Hall thruster but has resulted in erosion of the front magnetic field pole pieces. Recent experiments show that the erosion of graphite pole covers, which are added to protect the magnetic field pole pieces, causes carbon to redeposit on other surfaces, such as boron nitride discharge channel and cathode keeper surfaces. As a part of the risk-reduction activities for AEPS thruster development, this study models transport of backsputtered carbon from the graphite front pole covers and vacuum facility walls. Fluxes, energy distributions, and redeposition rates of backsputtered carbon on the anode, discharge channel, and graphite cathode keeper surfaces are predicted.

I. Introduction

HIGH-power solar electric propulsion has been identified as a critical part of an affordable, beyond-low-Earth-orbit manned-exploration architecture for NASA due to its substantially higher specific impulse than conventional chemical propulsion systems. Studies performed for NASA's Human Exploration and Operations Mission Directorate (HEOMD) and Science Mission Directorate have demonstrated that a 40 kW-class SEP capability can be enabling for both near term and future architectures and science missions.[1] Since 2012, NASA has been developing a 14 kW Hall thruster electric propulsion string that can serve as the building block for realizing a 40 kW-class SEP capability. NASA continues to evolve a human exploration approach to expand human presence beyond low-Earth orbit and to do so, where practical, in a manner involving international, academic, and industry partners.[2] NASA publicly presented a phased exploration concept at the HEOMD Committee of the NASA Advisory Council meeting on March 28, 2017.[3] NASA presented an evolutionary human exploration architecture, depicted in Fig. 1, to expand human presence deeper into the solar system through a phased approach including cis-lunar flight testing and validation of exploration capability before crewed missions beyond the earth-moon system and eventual crewed Mars missions. One of the key objectives is to achieve human exploration of Mars and beyond through the prioritization of those technologies and capabilities best suited for such a mission in accordance with the stepping stone approach to exploration.[4] High-power solar electric propulsion is one of those key technologies that has been prioritized because of its significant exploration benefits. A high-power, 40 kW-class Hall thruster propulsion system provides significant

---

[1] R&D Engineer, Electric Propulsion Systems Branch, maria.choi@nasa.gov.
[2] R&D Engineer, Electric Propulsion Systems Branch, john.t.yim@nasa.gov.
[3] R&D Engineer, Electric Propulsion Systems Branch, george.j.williams@nasa.gov.
[4] Ion Propulsion System Lead, Electric Propulsion Systems Branch, Daniel.a.herman@nasa.gov.
[5] Senior Scientist & Lead, Power, Propulsion and Communications Group, GRC Electric Propulsion Systems Branch, james.h.gilland@nasa.gov.

capability and represents, along with flexible blanket solar array technology, a readily scalable technology with a clear path to much higher power systems.

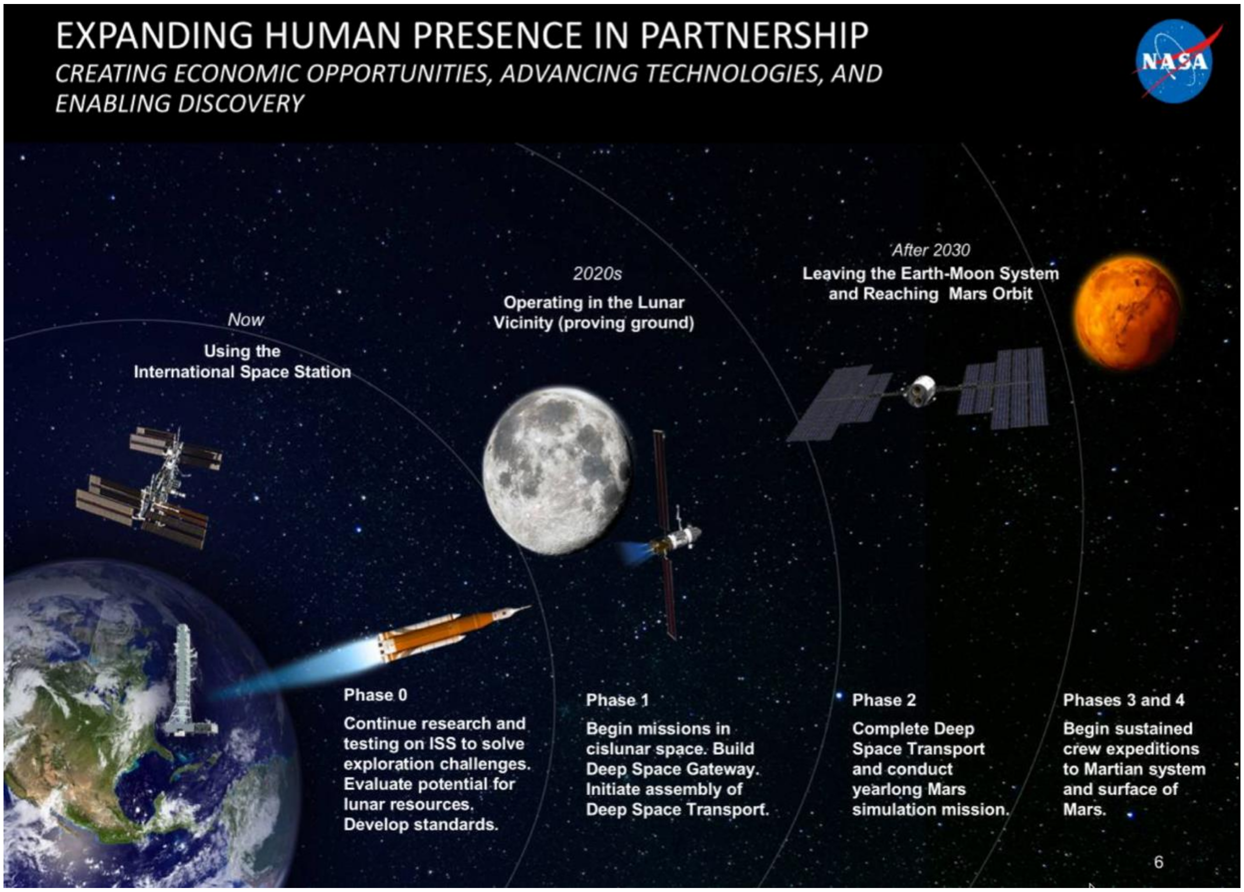

EXPANDING HUMAN PRESENCE IN PARTNERSHIP

CREATING ECONOMIC OPPORTUNITIES, ADVANCING TECHNOLOGIES, AND ENABLING DISCOVERY

Now
Using the International Space Station

2020s
Operating in the Lunar Vicinity (proving ground)

After 2030
Leaving the Earth-Moon System and Reaching Mars Orbit

Phase 0
Continue research and testing on ISS to solve exploration challenges. Evaluate potential for lunar resources. Develop standards.

Phase 1
Begin missions in cislunar space. Build Deep Space Gateway. Initiate assembly of Deep Space Transport.

Phase 2
Complete Deep Space Transport and conduct yearlong Mars simulation mission.

Phases 3 and 4
Begin sustained crew expeditions to Martian system and surface of Mars.

6

Figure 1. NASA Human Exploration Vision including Deep Space Gateway (DSG) and Deep Space Transport (DST).[5]

The 14 kW Hall thruster system development, led by the NASA Glenn Research Center (GRC) and the Jet Propulsion Laboratory (JPL), began with maturation of the high-power Hall thruster and power processing unit. The technology development work has transitioned to Aerojet Rocketdyne via a competitive procurement selection for the Advanced Electric Propulsion System (AEPS). The AEPS contract includes the development, qualification, and multiple flight 14 kW electric propulsion string deliveries. The AEPS Electric Propulsion (EP) string consists of the Hall thruster, power processing unit (including digital control and interface functionality), xenon flow controller, and associated intra-string harnesses. NASA continues to support the AEPS development leveraging in-house expertise, plasma modeling capability, and world-class test facilities. NASA also executes AEPS and mission risk reduction activities to support the AEPS development and mission application. An overview of the NASA and Aerojet development activities and mission application of the AEPS Hall thruster system is provided by Herman.[6]

While the lifetime of conventional Hall thrusters has been limited by the erosion of discharge channel walls, magnetic shielding in Hall thrusters[7,8] eliminated the discharge channel wall erosion as the primary failure mechanism of Hall thrusters. However, previous wear testing of magnetically-shielded Hall thrusters showed that the erosion of other surfaces was increased.[9,10,11,12] While the reduction in the discharge channel wall erosion in magnetically shielded Hall thrusters surpasses the relatively-slow increase in erosion rates in the front poles,[12] the erosion on the inner magnetic pole piece surface now constitutes to the primary erosion-based service life limiting mechanism. To reduce the risk of the magnetic circuit being eroded, the thruster design was updated to include front pole covers made of graphite—an erosion-resistant material. Despite the employment of erosion-resistant material, xenon ion bombardment on the graphite pole covers resulted in backsputtered carbon, and the rate at which carbon sputters from the inner front pole cover is now greater than the vacuum facility backsputter rate. Redeposition of these carbon particles has been observed on various parts of the thruster, including the anode, boron nitride discharge channel walls, and cathode keeper surfaces.[13] While the carbon population is still too low to affect thruster performance, it could affect how much carbon is getting to the thruster surfaces important for proper erosion determination and thruster lifetime assessment.

Since detailed understanding of ionization and redeposition rates of backsputtered carbon is of a great value added to the risk-reduction activities for HERMeS thruster development, the present study simulates transport of backtputtered carbon from both vacuum facility walls and graphite front pole covers of the thruster. In this paper, transport of carbon in the near-field plume and the inside discharge channel is modeled using the direct simulation of Monte Carlo combined with the particle-in-cell method. Backsputter rates from vacuum facility walls and the regression rates of front pole covers are measured and fed into the model as an input. Fluxes, energy distributions, and redeposition rates of carbon on various surfaces are predicted.

The erosion and performance characterization of the HERMeS observed in short duration tests are discussed in companion papers, Refs. 13 and 14, respectively. Other risk-reduction activities are currently on-going at NASA GRC and JPL, including surface layer activated wear testing,[15] extensive numerical modeling,[16] assessment of the impact of carbon deposition on service-life assessment,[17] and laser-based characterization of near-field ions.[18]

II. Carbon Transport Modeling Description

A. Numerical Model

The transport of backsputtered carbon is simulated using the two-dimensional axi-symmetric direct simulation of Monte Carlo (DSMC)-particle-in-cell (PIC) code developed by the University of Michigan.[19] Since carbon (C) densities are several orders of magnitudes smaller than xenon (Xe) densities (as shown in Figure 2), carbon will not make significant impact on plasma properties or thruster performance. Therefore, a time-averaged plasma simulation solution from JPL-developed Hall2De[16] is used to provide a fixed Xe plasma background flow. The electron temperature, electric fields, and the number densities and velocities of Xe plasma and electron are interpolated to the computational mesh and fixed constant in time. The current Hall2De solution contains three fluids for three xenon ion species, i.e., Xe^{+}, Xe^{2+}, Xe^{3+}, totaling nine Xe ion species.[16] The present study simulates atomic carbon neutrals (C) and ions (C^{+}), and does not include carbon clusters (e.g. C_2 and C_3), even though they may be important in backsputtering calculation.[26,27]

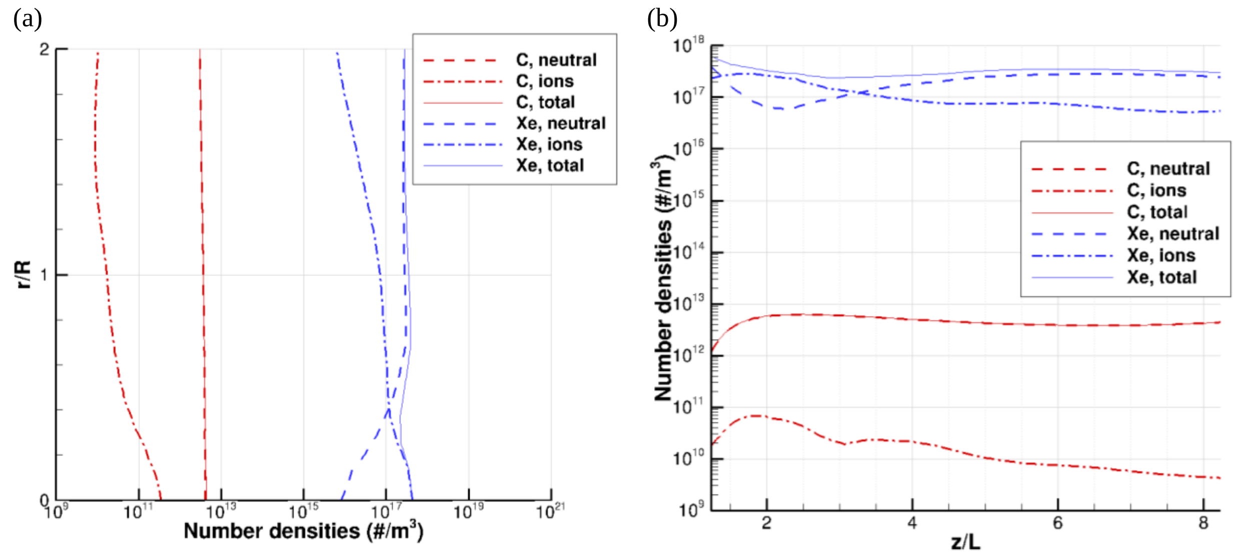

Figure 2: Comparisons of number densities of xenon vs. carbon extracted (a) in the radial direction just downstream of the front pole cover exit plane, and (b) in the axial direction along the channel centerline. Both plots show that total carbon density is approximately five orders of magnitudes lower than the total xenon number densities.

In this study, two basic classes of important collision mechanisms in Hall thrusters are implemented: the momentum exchange (MEX) and charge exchange (CEX) collisions. **Table 1** summarizes the detailed collision classes modeled in this study. The collisions between C-C and C-C^{+} are neglected due to their low densities (Figure 2).

Table 1: Collision classes modeled in this study.

	Xe	**Xe$^+$**	**Xe^{2+}**	**Xe^{3+}**	**C**	**C$^+$**
C	MEX	MEX, CEX	MEX	MEX	none	none
C$^+$	MEX, CEX	MEX	MEX	MEX	none	none

A list of colliding particle pairs in each cell are selected at random, regardless of their relative positions and velocities, to perform binary collisions. The collision probability of each pair is calculated at each time step, and is proportional to the product of the relative velocity between the colliding particles, g, and the total cross-section, σ. In each cell, the number of ionized particles and the total number of possible collision candidate pairs for each time step is calculated using Bird's No-Time-Counter.[20] For collision pair p and q, the number of collisions that can occur is:

$$N_{pq} = \frac{1}{2} N_p N_q (\sigma g)_{pq,max} \Delta t \tag{1}$$

where N is the local number density and Δt is the time step size. For all collision cross sections, the variable hard sphere (VHS)[21] model is employed. Once the collision probability is calculated, it is compared with a random number to determine whether a collision occurs or not. If a collision happens, the post-collision velocities are calculated using conservation of momentum and energy and assuming isotropic scattering. Only C and C$^+$ species properties are updated.

The model also includes the electron-impact ionization of carbon neutrals. For the ionization cross section, this study uses modified Young's formula[22]:

$$\sigma_{i,(C)} = \frac{\alpha}{\left(u + \frac{E_i}{\pi}\right) E_i^2} \left[A\left(1 - \frac{1}{u}\right) + B\left(1 - \frac{1}{u}\right)^2 + C\ln(u) + \frac{D}{u}\ln(u) \right] \tag{2}$$

where $u = T_e/E_i$, and T_e is the electron temperature, E_i is the ionization potential, and α and A-D are the fitting coefficients to fit Brook's ionization data[23], as defined in Table 2. The resulting ionization cross section curve is shown in Figure 3.

Table 2: Parameters used in this study for Eq. (2) to fit Brook's electron impact ionization data[24] for carbon.

α	$E_i\ (eV)$	A	B	C	D
360.0	11.26	12.2	-3.91	1.85	-10.3

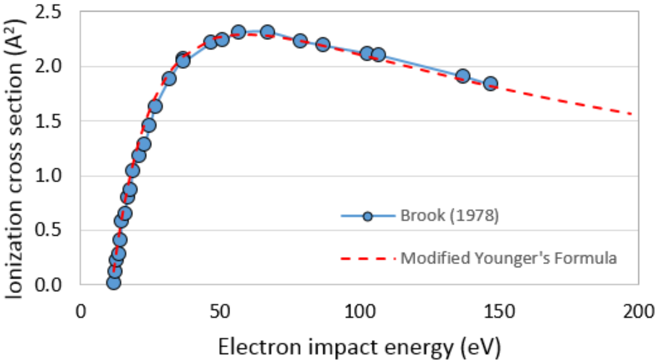

Figure 3: Electron impact ionization cross section for carbon atom.

B. Computation Domain and Boundary Conditions

The computation domain is shown and labeled in Figure 4, which includes near-field plume and discharge channel regions. The domain consists of 3500 cells, and about 0.9 million carbon macroparticles are used. Carbon neutrals are introduced from the inner front pole cover (IFPC), the outer front pole cover (OFPC), and the axial and radial far-field boundaries. No flow is introduced from the anode or the cathode, as plasma properties from a Hall2De solution are fixed in the background.

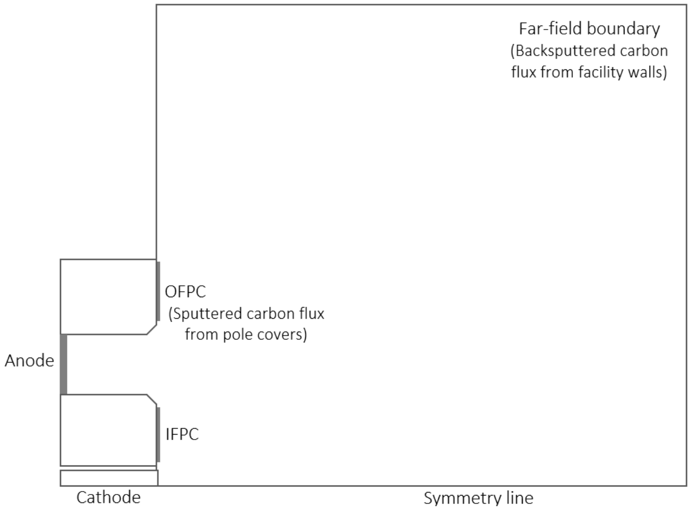

Figure 4: 2-D axisymmetric computational domain and labels on each boundary (not drawn to scale). Carbon atoms are introduced on the inner and outer front pole covers and the far-field boundaries (top and right).

The fluxes of carbon backsputtered from front pole covers are based on the Technology Demonstration Unit 1 (TDU-1) wear test measurement.[11] During the short-duration wear test of TDU-1 in VF-5 at the nominal 600 V, 12.5 kW operating condition, the net erosion rates of the IFPC was approximately 25.0 μm/khr, and no measurable erosion/deposition was measured from the OFPC. The fluxes of carbon backsputtered from the VF-5 chamber walls are based on the quartz crystal microbalance (QCM) data.[17] The mean backsputter rate in the axial direction measured by QCM for this test was approximately 1.8 μm/khr, and the radial direction is assumed to be about 20 % of the axial rate, based on our recent measurement. Assuming that all facility backsputter carbon particles stick to the graphite front pole covers during this operation, the fluxes of carbon atoms introduced in the computation domain are summarized in Table 3. Although the axial far-field boundary is not at the QCM location, the backsputter rate at the far-field boundary is assumed to be equivalent to the rate at the QCM location, which is at the thruster exit plane. The chamber backpressure during this operation was approximately 4.6E-6 Torr, corrected for Xe.

Table 3: Number fluxes ($m^{-2}s^{-1}$) of carbon atoms at each inflow boundary.

IFPC	OFPC	Axial far-field	Radial far-field
8.4×10^{17}	5.7×10^{16}	5.7×10^{16}	1.1×10^{16}

The energy, E, of sputtered particles from a surface is characterized using the well-known Sigmund-Thompson energy distribution[25]:

$$f_E \propto \frac{E}{(E + U_b^2)^{3-2m}} \tag{3}$$

where $U_b = 7.4$ eV is the binding energy, and $m = 1/3$ is the interatomic potential exponent parameter. This distribution normalized by its area is shown in Figure 5, and has the most probable energy of 5.6 eV. In order to simplify the modeling process, particles are sampled using the Maxwellian velocity distribution functions (VDFs) with the same most probable energy as a first approximation (shown in blue dashed curve in Figure 5). By matching the most probable energies of both distributions, the spread in the Maxwellian distribution is much narrower and the peak is about 2.5 times higher than Sigmund-Thompson distribution. This means that, by making the assumption of Maxwellian VDF, we are under-estimating carbon atoms with higher energies, and over-estimating carbon atoms with lower energies. However, this under- and over-estimation of higher and lower energy carbon atoms, respectively, has a negligible effect on the total collision cross sections, since carbon energy is very low compared to the beam ion energy.

In classical theory, the angular distribution of sputtered particles follow cosine distribution, as shown in the blue curve of the polar plot, Figure 6(a). Experimental measurements of differential sputter yields show that particles are sputtered following under-cosine profile,[26,27,28] such as Figure 6(b). The angular distribution of sputtered particles becomes more cosine-like when the incidence energy is lower.[28] The expected energy range of incident xenon ions are in the low ranges (< 100 eV) for the IFPC,[13] which makes the cosine distribution a reasonable assumption for a first approximation. On the other hand, because the far-field boundary of the simulation is still far away from the actual vacuum chamber walls, uniform angular distribution is assumed, as shown in the red curve in Figure 6(b).

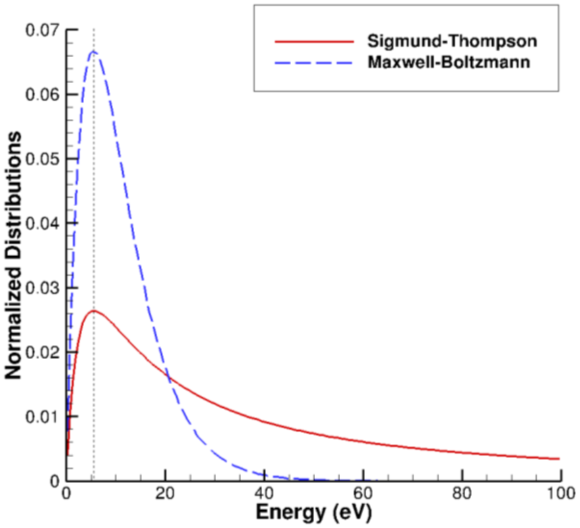

Figure 5: Comparison of the Sigmund-Thompson distribution (red) and the sampled energy distribution for backsputtered carbon, assuming Maxwellian vdf (blue). By matching the most probable energy of 5.6 eV, carbon with higher energies and lower energies are under-estimated and over-estimated, respectively.

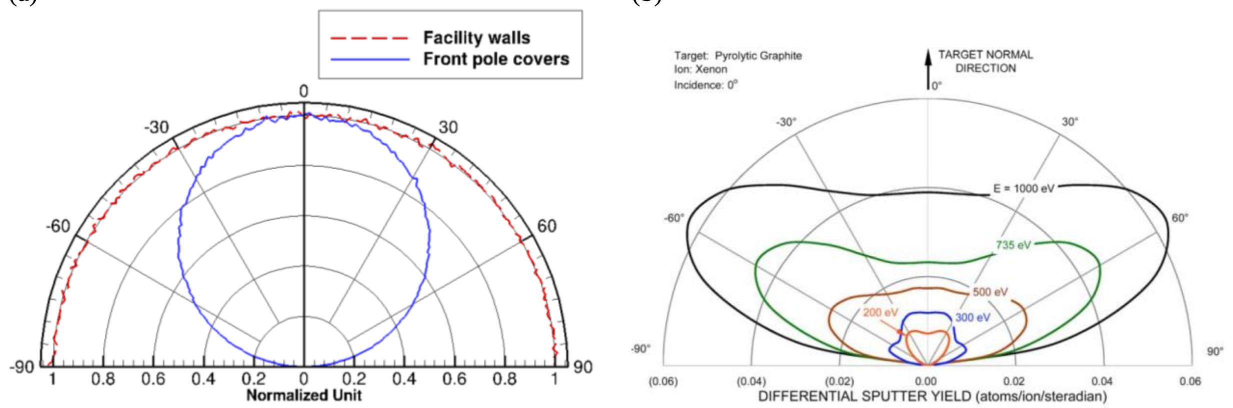
(a)

(b)

Figure 6: Polar plots of the angular distributions of (a) sampled carbon atoms at the IFCP in the simulation and (b) measurement from Ref. [28].

When carbon particles hit surfaces, they are assumed to reflect diffusely. The temperature of all surfaces are assumed as 900 K. The sticking coefficients for the anode, the boron nitride (BN) discharge channel, and the graphite cathode keeper are 0.65, 0.99, and 0.99, respectively. Once a carbon coating is formed, the sticking will be as for a carbon surface. Therefore, since this study is concerned with a wear test, the sticking coefficient of 0.99 is used also for the anode surface. Lastly, no carbon clusters (e.g. C_2 and C_3) are modeled for the present work, even though they may be important in backsputtering calculation.[26,27]

III. Results and Discussions

In this section, steady-state results of carbon transport simulation are presented. The backsputtered carbon species from the facility walls and the IFPC and OFPC are separately tracked in the model to quantify redeposition amounts of species on various surfaces.

A. Simulation Results

Figure 7(a) shows the generation of carbon ion particles, and the legend represents the number of macro ions generated during the simulation. The purpose of this plot is to indicate the locations of where carbon atoms get ionized, which are in the acceleration/ionization region and downstream of the cathode plume region. Recalling Eq. (1) and (2), the carbon ion generation in these regions corresponds to the regions of high electron temperature and electron number densities. Figure 7(b)-(d) shows time-averaged Hall2De solution of electron temperature, number density, and plasma potential, respectively, interpolated on the computational grid used in this study for 600 V, 12.5 kW nominal condition.

(a) Generation of carbon ions (b) Electron temperature

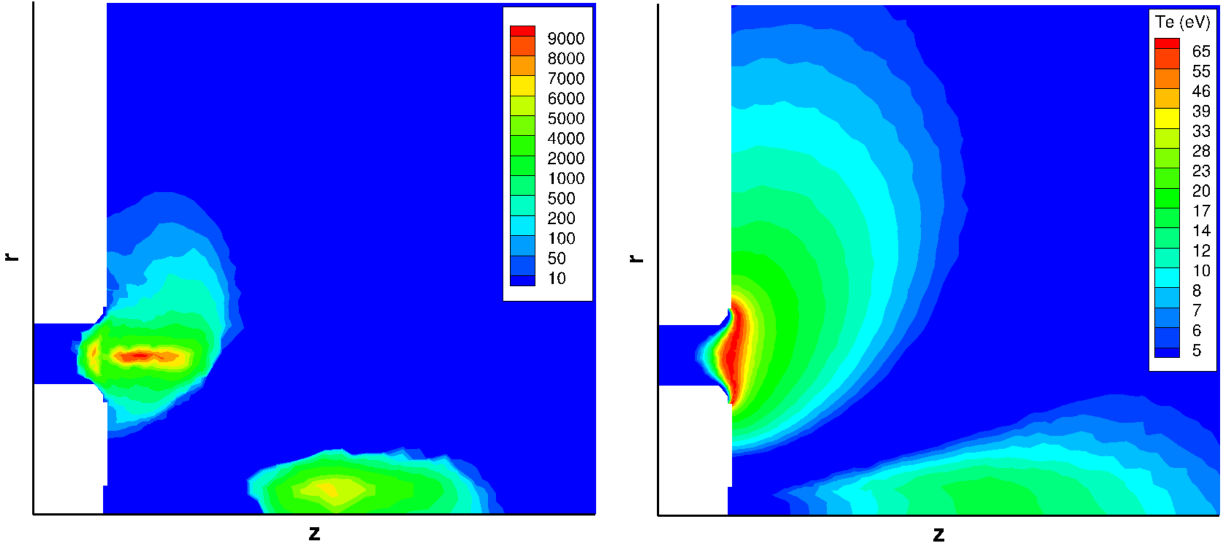

(c) Electron density (d) Plasma potential

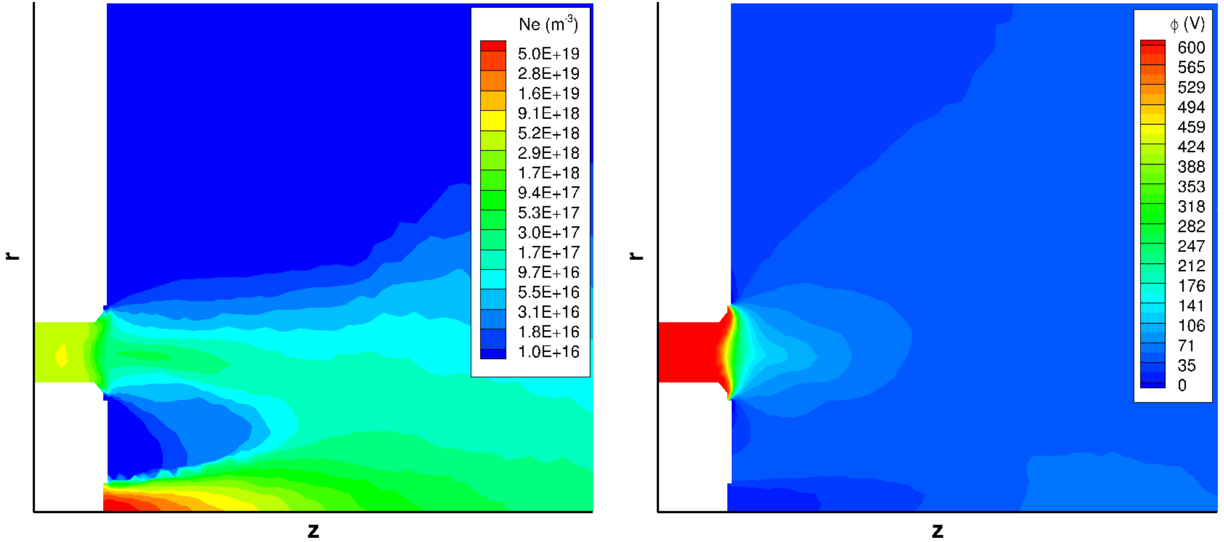

Figure 7: Contour plots of (a) generation of carbon ions calculated from MPIC, and (b) electron temperature, (c) electron number density, and (d) plasma potential, calculated by Hall2De.

The carbon neutral and ion number densities are plotted in Figure 8(a) and 9(a), respectively. The carbon neutral density ranges from 2.8E11 to 4.4E13 m^{-3} in the computational domain, while carbon ion density ranges from 1E5 (minimum density) to 1.7E12 m^{-3}. Figure 8(b)-(d) show the number densities of carbon neutrals from the IFPC, the OFPC, and facility walls, respectively. When carbon atoms are generated at these inflow boundaries, they move with their initial velocities until they undergo collisions with the background xenon species, whether Xe neutrals or ions. Carbon neutral densities from both the IFPC and OFPC decrease away from the pole surfaces monotonically with spherical shape. The facility backsputter carbon density also decreases monotonically from the top and right far-field boundaries due to collisions with the plasma. In previous backsputter carbon modeling effort, [17] non-uniform carbon fluxes in the vacuum chamber was predicted using the Hypersonic Aerothermodynamics Particle (HAP) code.[29] Still, the decrease in the carbon number density predicted in this study is higher than expected. While some of this reduction in the density may be physical, sensitivity studies are currently underway to examine whether this is a result of isotropic assumption and small domain.

When these backsputtered carbon neutrals collide with electrons, mostly in the acceleration/ionization region by the channel as seen in Figure 7(a), they are ionized. Then, carbon ions are accelerated in the direction of electric field, calculated by the negative gradient of the plasma potential from Figure 7(d). In Figure 9, the number densities of the IFPC, the OFPC, and facility carbon ions are plotted. Some of the ions born in the acceleration/ionization region are accelerated downstream, following the axial electric field, and some follow the radial potential drop towards the cathode, resulting in the highest carbon ion densities along the cathode centerline, as shown in Figure 9. The carbon ions generated downstream of the cathode plume also migrates upstream towards the cathode, following the axial electric field pointing towards the cathode.

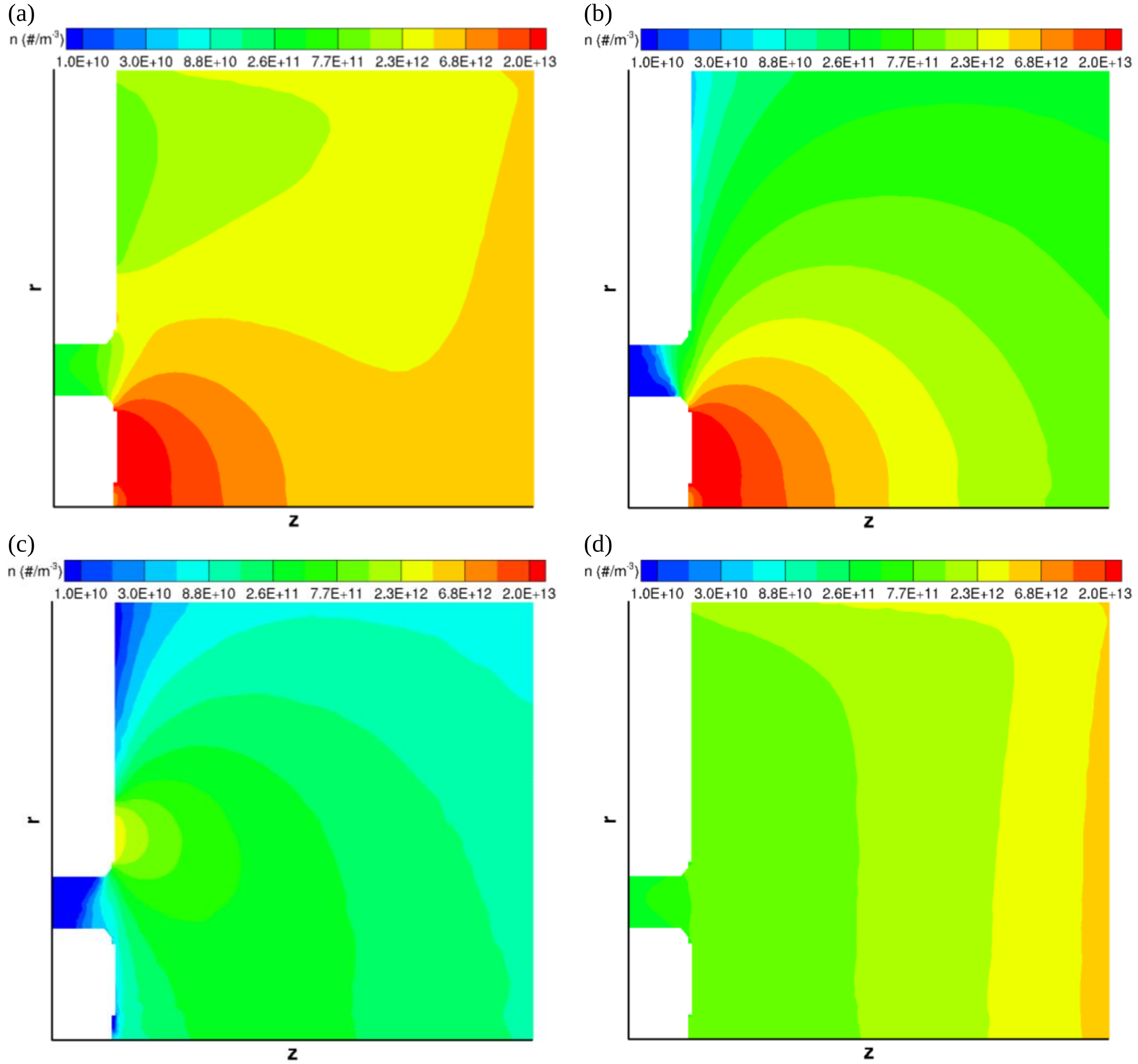

Figure 8: Number densities of (a) the total carbon atoms, (b) the IFPC carbon atoms, (c) OFPC carbon atoms, and (d) facility backsputter carbon atoms.

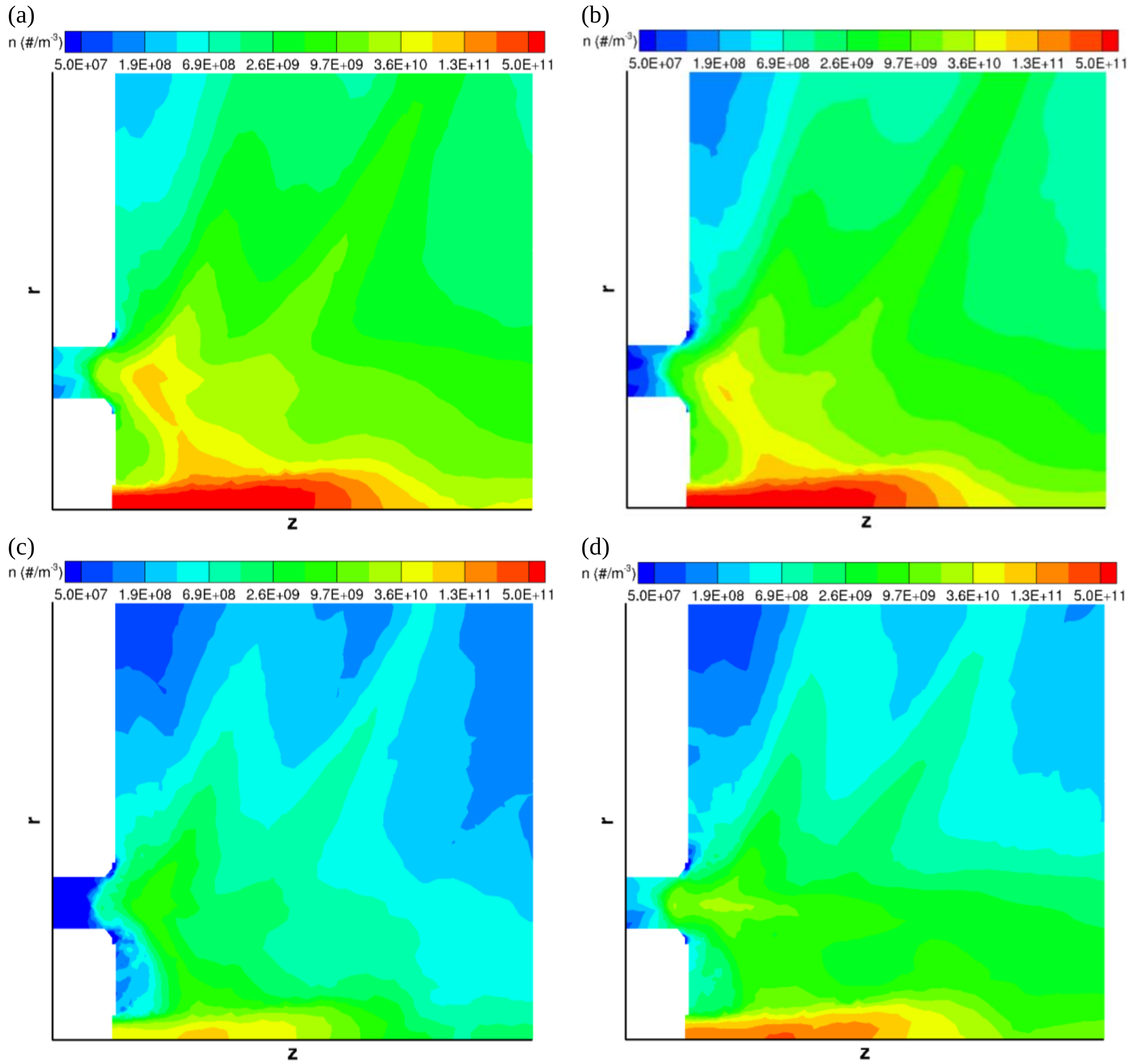

Figure 9: Number densities of (a) the total carbon ions, (b) the IFPC carbon ions, (c) OFPC carbon atoms, and (d) facility backsputter carbon ions.

Figure 10 shows the fluxes of backsputtered carbon arriving on the BN inner and outer discharge channel surfaces. The discharge channel wall is divided into three parts for closer examination, which are the main channel wall, chamfer, and front flat parts as shown in Figure 10 (a). On the main channel wall and the chamfer of the inner channel (IC), the deposited carbon flux is dominated by carbon from the far-field boundaries, which represent the vacuum facility backsputter carbon neutrals. On the front flat part of the IC, the carbon flux from the IFPC surpasses the facility carbon flux. There is either no or very small amount of carbon ions along both inner and outer channels, because ions follow the local electric field and thus are accelerated out the thruster immediately after they are born. In Figure 10(b), from the anode side to the mid-length of the outer channel (OC) wall shows a similar amount of facility backsputter carbon neutral flux as seen in the IC wall. However, from the mid-channel wall to the chamfer, the carbon neutral flux from the IFPC increases to comparable magnitudes of the facility carbon neutrals. The OFPC carbon neutral flux rapidly increases on the front flat of the channel.

Figure 11 shows the fluxes of carbon redeposited on the anode and cathode surfaces. The carbon flux on the anode is dominated by facility backsputter carbon neutrals. On the front surface of the cathode keeper, large amounts of carbon neutrals and ions from the IFPC are deposited, surpassing the amount of facility backsputtered carbon. There are also large amounts carbon ions hitting the keeper surface. These high ion fluxes can be explained by high ion number densities (Figure 9) and negative potential gradient (Figure 7(d)) previously discussed. The energy distribution of depositing carbon particles is examined to determine its full effects on the cathode keeper.

Figure 12(a) shows the energy distributions collected on the IC, OC, cathode, and anode surfaces. For all surfaces except the cathode keeper, energy distributions are mostly preserved from the beginning-of-life (BOL) energy distributions. The highest populations are shown around 5-7 eV, which is their most probable energy at birth matching the Sigmund-Thompson distribution, implying that the carbon species arriving at these surfaces did not undergo collisions. For the cathode keeper surface, a higher peak around 30-45 eV is added to its BOL distribution. This higher energy peak is predominantly from carbon ions backsputtered from all surface, as shown in Figure 12(b). Carbon ions gain this energy by accelerating through the potential drop towards the cathode. Currently, no sputter yield data is found for carbon ions striking a graphite surface with energies of 30-45 eV, to the best of our knowledge. Thus, more investigation is required to determine whether these ions would or would not cause any erosions on the graphite keeper surface.

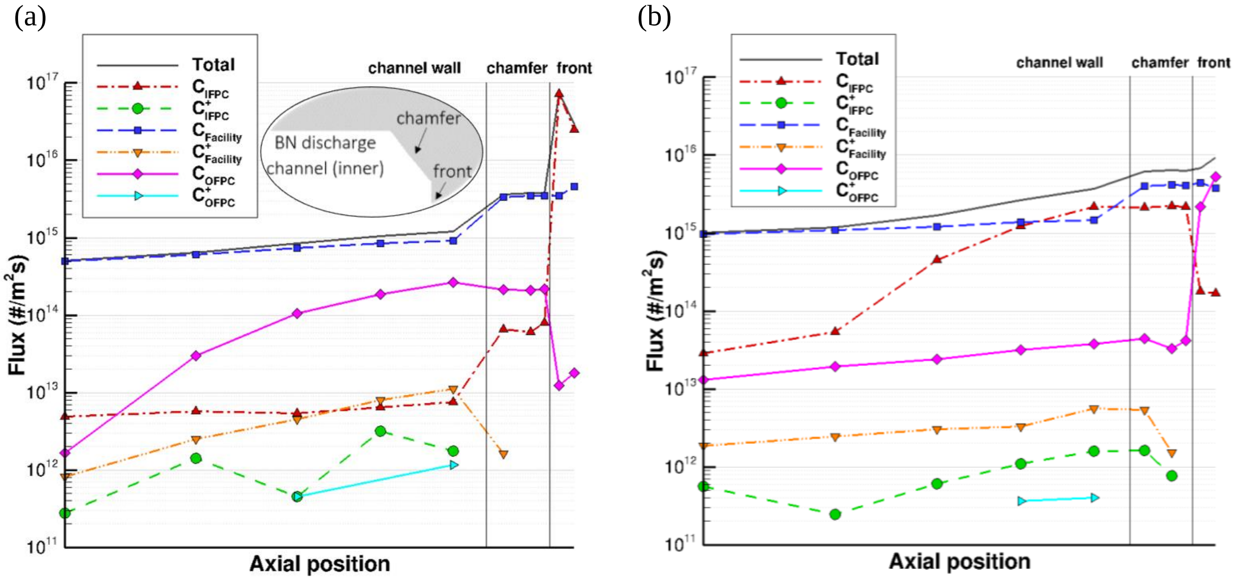

Figure 10: Fluxes of backsputtered carbon redepositing on the inner channel (left) and outer channel (right) surfaces.

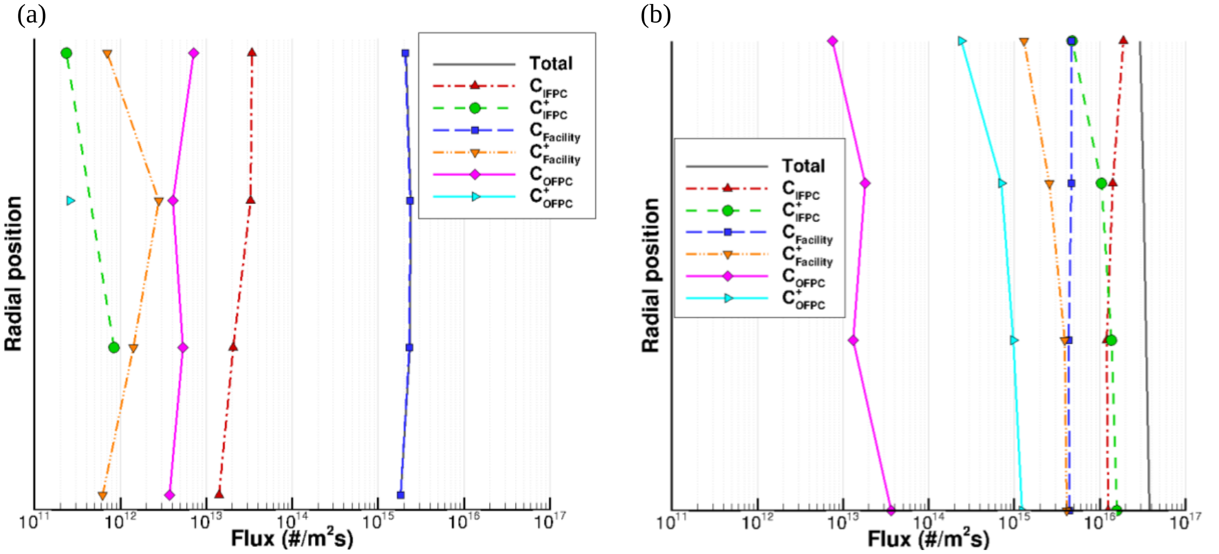

Figure 11: Fluxes of backsputtered carbon redepositing on (a) the anode and (b) the cathode surfaces.

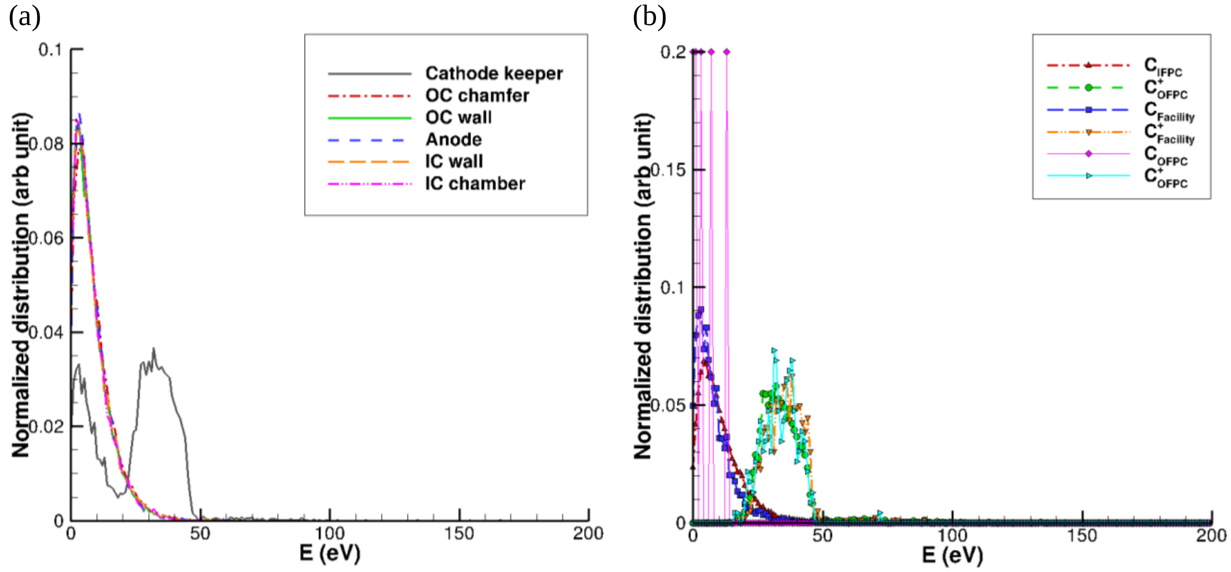

Figure 12: (a) Energy distributions of backsputtered carbon redepositing on all surfaces, and (b) energy distributions of individual carbon species redepositing on the cathode keeper surface.

IV. Summary and conclusion

As a part of the risk-reduction activities for AEPS thruster development, the present study simulated transport of backsputtered carbon from the vacuum facility walls and graphite front pole covers of the thruster. While carbon density is much lower than Xe plasma and neutral densities, the ionization and redeposition were of interest for proper lifetime prediction and contamination modeling purposes. Based on the model used in this study, a few important conclusions were made. The redeposition of carbon from the front pole covers on the anode and the main discharge channel wall is mainly dominated by the facility backsputter carbon neutrals, which is up two orders of magnitudes higher than the pole cover carbon fluxes. However, the chamfer and front flat parts of the discharge channels have high carbon fluxes from the front pole covers, which is more than an order of magnitude larger than facility carbon flux in some regions. Finally, the cathode keeper collects high fluxes of carbon from both the front pole surfaces and the facility walls. The redeposition rates calculated from the flux of total carbon particles collected at the cathode keeper surface are approximately 0.8 μm/khr. Unfortunately, the net carbon erosion/redeposition rate measurement on the cathode of TDU-1 wear test in VF-5 was too low to be resolved to validate this result.

The energy distributions of carbon neutrals and ions arriving at the anode and discharge channel surfaces preserved their BOL energy distributions, implying that they have undergone no or little collisions. At the cathode keeper surface, the peak energy of carbon ions were found to be around 30-40 eV. Since there is no sputter yield data on carbon on graphite surfaces, it is not clear whether this will be a concern.

Future work may include the effects of molecular carbon species—such as C_2 and C_3—expanding this model and estimating carbon depositions on other important parts of the thruster, such as shock isolators, and applying the flux of carbon emanating from pole covers to spacecraft integration model for spacecraft contamination concerns.

Acknowledgments

The authors would like to like to thank the Space Technology Mission Directorate through the Solar Electric Propulsion Technology Demonstration Mission Project for funding the joint NASA GRC and JPL development of the Advanced Electric Propulsion System. The authors also would like to thank Alejandro Lopez Ortega at JPL for providing Hall2De simulation.

References

[1]Smith, B. K., Nazario, M. L., and Cunningham, C. C., "Solar Electric Propulsion Vehicle Demonstration to Support Future Space Exploration Missions," Space Propulsion 2012, Bordeaux, France, May 7-10, 2012.

[2]Congress, "National Aeronautics and Space Administration Transition Authorizatin Act of 2017," 2017.

[3]HQ, N., "Meeting Agenda and Minutes," NASA Advisory Council Human Exploration and Operations Committee Meeting, https://www.nasa.gov/sites/default/files/atoms/files/nac_heoc_march_2017_public_agenda_revb.pdf, [cited March 28, 2017].

[4]Gerstenmaier, W., "Progress in Defining the Deep Space Gateway and Transport Plan," NASA Advisory Council Human Exploration and Operations Committee Meeting, https://www.nasa.gov/sites/default/files/atoms/files/nss_chart_v23.pdf, [cited March 28, 2017].

[5]Gerstenmaier, Bill, "Progress in Defining the Deep Space Gateway and Transport Plan," https://www.nasa.gov/sites/default/files/atoms/files/nss_chart_v23.pdf, NASA Advisory Council Human Exploration and Operations Committee Meeting, March 28-29, 2017, NASA Headquarters, Washington, D.C.

[6]Herman, D. A., et al., "Overview of the Development and Mission Application of the Advanced Electric Propulsion System (AEPS)," 35th International Electric Propulsion Conference, IEPC-Paper 2017-384, October, 2017.

[7]Mikellides, I., Katz, I., Hofer, R., Goebel, D., "Magnetic shielding of the channel walls in a Hall plasma accelerator," *Physics of Plasmas*, 18, (2011): 033501.

[8]Hofer, R. R., Goebel, D., Mikellides, I. G., and Katz, I., "Design of a Laboratory Hall Thruster with Magnetically Shielded Channel Walls, Phase II: Experiments," 48th AIAA/ASME/SAE/ASEE Joint Propulsion Conference and Exhibit, AIAA-2012-3788, Atlanta, GA, July 2012.

[9]Hofer, R. R., Jorns, B. A., Mikellides, I. G., Snyder, J. S., "Wear Test of a Magnetically Shielded Hall Thruster at 3000s Specific Impulse," IEPC-2013-033, 33rd International Electric Propulsion Conference, Washington D.C., Oct. 6-10, 2013.

[10]Goebel D. M., Jorns, B. A., Hofer, R. R., Mikellides, I. G., and Katz, I., "Pole-piece interactions with the plasma in a magnetically shielded Hall thruster," 50th *AIAA/ASME/SAE/ASEE Joint Propulsion Conference and Exhibit*, Cleveland, OH, July 28-30, 2014.

[11]Williams, G. J., Gilland, J. H., Peterson, P. Y., Kamhawi, H., Huang, W., Swiatek, M., Joppeck, C., Yim, J. T., and Haag, T. , "2000-hour Wear-Testing of the HERMeS Thruster," 52nd *AIAA/ASME/SAE/ASEE Joint Propulsion Conference*, Salt Lake City, UT, July 25-27, 2016.

[12]Sekerak, M., Hofer, R. R., Polk, J. E., Jorns, B. A., and Mikellides, I. G., "Wear testing of a magnetically shielded hall thruster at 2000 s specific impulse," 34th International Electric Propulsion Conference, Kobe, Japan, July 2015.

[13]Williams, G. J., Gilland, J. H., Kamhawi, H., Choi, M., Peterson, P. Y., Herman, D. A., "Wear Trends of the HERMeS Thruster as a Function of Throttle Point," 35th *International Electric Propulsion Conference*, Atlanta, GA, Oct. 8-12, 2017.

[14]Kamhawi, H., Gilland, J. H., Williams, Mackey, J., Hunag, W., Haag, T., and Herman, D. A., "Performance and Stability Characterization of the HERMeS Thruster with M26 Boron Nitride Discharge Channel," 35th *International Electric Propulsion Conference*, Atlanta, GA, Oct. 8-12, 2017.

[15]Polk, J. E., Lobbia, R. B., Barriault, A., Chaplin, V., Ortega, A. L., Mikellides, I. G., "Inner Front Pole Erosion in the 12.5 kW HERMeS Hall Thruster Over a Range of Operating Conditions," 35th *International Electric Propulsion Conference*, Atlanta, GA, Oct. 8-12, 2017.

[16]Ortega, A. L., Mikellides, I. G., Chaplin, V., "Hall2De Simulations for the Assessment of Pole Erosion in the 12.5 kW Hall Effect Rocket with Magnetic Shielding (HERMeS)," 35th *International Electric Propulsion Conference*, Atlanta, GA, Oct. 8-12, 2017.

[17]Gilland, J. H., Williams, G. J., Burt, J. M., and Yim, J. T., "Carbon Back Sputter Modeling for Hall Thruster Testing", 52nd *AIAA/SAE/ASEE Joint Propulsion Conference*, Salt Lake City, UT, July 25-27, 2016.

[18]Jorns, B. A., Dodson, C., Anderson, J., Goebel, D. M., Hofer, R.R., Sekerak, M. J., Ortega, A. L., and Mikellides, I. G., "Mechanisms for Pole Piece Erosion in a 6-kW Magnetically-Shielded Hall Thruster," 52nd *AIAA/SAE/ASEE Joint Propulsion Conference*, Salt Lake City, UT, July 25-27, 2016.

[19]Cai, C., "Theoretical and numerical studies of plume flows in vacuum chambers," Ph.D. Dissertation, Department of Aerospace Engineering, University of Michigan, Ann Arbor, MI, 2005.

[20] Bird, G. A. (1994). Molecular gas dynamics and the direct simulation of gas flows.

[21]Bird, G. A., "Monte-Carlo simulation in an engineering context," *Progress in Astronautics and Aeronautics, 74* (1981): 239-255.

[22]Younger, S. M. "Electron impact ionization cross sections and rates for highly ionized atoms." Journal of Quantitative Spectroscopy and Radiative Transfer 26.4 (1981): 329-337.

[23]Brook, E., M. Harrison, F. A. and Smith, A. C. H., "Measurements of the electron impact ionisation cross sections of He, C, O and N atoms," *Journal of Physics B: Atomic and Molecular Physics* 11.17 (1978): 3115.

[24]Brook, E., M. Harrison, F. A. and Smith, A. C. H., "Measurements of the electron impact ionisation cross sections of He, C, O and N atoms," *Journal of Physics B: Atomic and Molecular Physics* 11.17 (1978): 3115.

[25]Sigmund, P., "Sputtering by Ion Bombardment: Theoretical Concepts," Sputtering by Particle Bombardment I: Physical Sputtering of Single-Element Solids," edited by R. Behrisch, Vol. 47 of Topics in Applied Physics, Springer-Verlag, New York, 1981.

---

[26] Oyarzabel, J., Yu, J., Hanna, J., Tynan, G., Doerner, R., Taylor, K. and Schmid, K., "Molybdenum and carbon cluster angular sputtering distributions under low energy xenon ion bombardment," 41st *AIAA/ASME/SAE/ASEE Joint Propulsion Conference*, October, 2005.

[27] Oyarzabal, E., Doerner, R.P., Shimada, M. and Tynan, G.R., "Carbon atom and cluster sputtering under low-energy noble gas plasma bombardment," *Journal of Applied Physics*, 104(4), 2008.

[28] Williams, J. D., Johnson, M. L., and Williams, D. D., "Differential sputtering behavior of pyrolytic graphite and carbon-carbon composite under xenon bombardment," 40th *AIAA/ASME/SAE/ASEE Joint Propulsion Conference*, Fort Lauderdale, FL, July 11-14, 2004.

[29] Burt, J. M., E. Josyula, and I. D. Boyd. "Novel Cartesian Implementation of the Direct Simulation Monte Carlo Method," Journal of Thermophysics and Heat Transfer, Vol. 26, No. 2 (2012), pp. 258-270.